3-D stochastic finite elements for thermal creep analysis of piping structures with spatial material inhomogeneities

Appalanaidu, Y.; Roy, Anindya; Gupta, Sayan

DOI
10.1007/s00707-017-1865-9

Publication date
2017

Document Version
Final published version

Published in
Acta Mechanica

Acta Mech
DOI 10.1007/s00707-017-1865-9

ORIGINAL PAPER

Y. Appalanaidu · Anindya Roy · Sayan Gupta

3-D stochastic finite elements for thermal creep analysis of piping structures with spatial material inhomogeneities

Received: 31 October 2016 / Revised: 18 March 2017

Abstract A stochastic finite element-based methodology is developed for creep damage assessment in pipings carrying high-temperature fluids. The material properties are assumed to be spatially randomly inhomogeneous and are modelled as 3-D non-Gaussian fields. A spectral-based approach for random field discretization that preserves exactly the non-Gaussian characteristics is used in developing the stochastic finite element model. The meshing used in random field discretization is distinct from FE meshing, depends on the correlation characteristics of the random fields and is computationally efficient. The methodology enables estimating the failure probability and the most likely regions of failure in a section of a circular pipe.

1 Introduction

Thermal creep is a dominant damaging mechanism in piping structures that carry high-temperature liquids in industrial installations, especially in nuclear power plants. The fatal consequences of failure in these piping components lead to extreme conservatism in design and maintenance scheduling. A consequence of this conservatism in design requires replacing/retrofitting often structurally safe components but which have exceeded their so-called design life. This has an adverse effect on the financial burden of the plants. This conservative approach to design and maintenance is an acknowledgement of the uncertainties that invariably exist in numerical modelling of the loading and the material properties and which are not accounted for in traditional design procedures.

The focus of this study is primarily on investigating the effects of the random inhomogeneities in the material properties on thermal creep damage growth in structural components with long exposure to high-temperature environment using stochastic finite element method. The spatial uncertainties exhibited in the macroscopic material properties are due to the inherent material micro-structural inhomogeneities that result from the unavoidable fluctuations in complex manufacturing processes. This, in turn, affects the structural capacity to withstand the thermal loads and explains the scatter in the creep life times that has been experimentally observed on identical specimens under identical loadings [1]. Recently developed alternative design strategies

Y. Appalanaidu · S. Gupta (✉)
Department of Applied Mechanics, Indian Institute of Technology Madras, Chennai 600036, India
E-mail: gupta.sayan@gmail.com
Tel.: +91 44 2257 4055
Fax: +91 44 2257 4052

Y. Appalanaidu
E-mail: appusir@gmail.com

A. Roy
Department of Civil Engineering, Technical University of Delft, Stevinweg 1, PO Box 5048, 2600 GA Delft, The Netherlands
E-mail: aroy.iitk@gmail.com

Published online: 19 May 2017

are based on probabilistic frameworks where the effects of the material and load uncertainties are explicitly modelled and incorporated into the analysis. This has opened up new challenges in the treatment of the uncertainties in the material properties in the analysis and the associated computational costs, especially in the context of complicated engineering structures where the finite element (FE) method is necessary for building numerical models. The challenge lies in adopting appropriate probabilistic models for the material property uncertainties that can be integrated with the structure FE models. Modelling the uncertainties as random variables is conceptually simpler and leads to easy integration with existing FE models. However, random variable models implicitly assume homogenization of the properties along the spatial extent of the subdomains of the structure and introduce epistemic uncertainties into the mathematical model which undermines the accuracy of the predictions. More accurate representation of the spatial uncertainties in the material properties can be incorporated by adopting random field models. However, incorporating random field models with FE models requires the development of alternative mathematical formulations—a crucial step of which lies in developing weak form representations for the random fields that enable them to be adopted within FE frameworks. This constitutes the basis of the subject of stochastic finite element method (SFEM). Discussions and literature review on the various methods of random field discretization and weak form representations are available in [2–9]. An important issue in most SFEM studies is that the random field descriptions are limited to second-order characteristics.

The treatment of Gaussian fields within the context of SFEM is relatively straightforward. However, Gaussian field models are not suitable for modelling physical parameters as there exists a finite probability of the properties attaining physically impossible negative values. Adopting non-Gaussian models for the fields, however, lead to complications in preserving the second-order non-Gaussian characteristics in the weak form representations. In this context, spectral-based approaches are observed to lead to efficient and accurate weak form representations for non-Gaussian fields. The underlying principle of these approaches lies in decomposing the non-Gaussian field into a mathematical subspace spanned by a set of orthogonal basis functions derived from the correlation function [3,8]. This leads to a weak form representation where the basis functions are in terms of polynomial functions of independent and identically distributed (i.i.d.) random variables whose probability density function (pdf) depends on the non-Gaussianity of the random field. An appropriate selection of the basis functions leads to an optimal series representation—known as polynomial chaos expansion (PCE)—which in turn leads to a minimum number of random variables entering the SFEM formulation. PCE representation of non-Gaussian random fields has been extensively studied for 1-D cases, but extending them to higher dimensions is not straightforward.

An alternative series representation for non-Gaussian random fields—the optimal linear expansion (OLE)—presents certain advantages in implementation. OLE as a tool for random field discretization was proposed in [10] primarily for Gaussian random fields. The applicability of OLE in the discretization of 1-D non-Gaussian random fields was discussed later in [11,12]. The advantages of OLE—as will be demonstrated in this study—are that the discretized random fields preserve their non-Gaussian characteristics exactly at the random field nodal points and its ease in implementation for higher-dimension fields as well as in non-rectangular spatial domains. More discussions on the advantages of the OLE approach in comparison to PCE are presented later in this paper.

The present study develops a 3-D SFEM-based methodology for investigating the stochastic growth of thermal creep damage in materials exposed to high-temperature environment. The crux in this study lies in representing the spatial random variability in material properties in curvilinear domains using OLE. This has necessitated the development of shape functions with topological features similar to the topology of the spatial domain. To the best of the authors' knowledge, SFEM-based studies on such complex curvilinear domains have not been attempted in the literature; implementation of PCE in these domains would be cumbersome and not easy either. The advantage of adopting the proposed OLE-based approach for representing the spatial random variability in material properties from sample experimental observations is also discussed. Subsequently, the growth of stochastic creep damage—a highly nonlinear phenomenon—is analysed using principles of continuum damage mechanics in a computationally efficient manner. Additional complications arising due to the thermal conductivity being modelled as a random field are addressed as well. Finally, a time-variant reliability analysis is carried out for estimating the failure probability and identifying the most likely regions of failure.

The paper is organized as follows: the problem considered in this paper is defined in Sect. 2. Section 3 is devoted to the development of OLE discretization of 3-D non-Gaussian random fields and characterizing the errors in the weak form representation. The formulation of the SFEM approach as applicable for cylindrical piping systems is developed in Sect. 4. The methodology for failure probability estimation is discussed in

Sect. 5. Section 6 presents a discussion on the development of the OLE-based representation for a random field based on discrete sample measurements of a sample realization of a random field. Section 7 presents a suite of numerical results that highlight the developments proposed in this paper. A discussion on the advantage of using the OLE-based approach vis-a-vis existing spectral-based methods such as the KL expansion and PCE is presented in Sect. 8. The salient features of the proposed method that emerge from this study are summarized in Sect. 9. An "Appendix" is provided at the end which details the thermal creep damage growth equations considered in the analysis.

2 Problem statement

A long section of a cylindrical pipe carrying high-temperature fluid is considered for the analysis. The fluid is assumed to completely fill the pipe and exerts a constant pressure P acting along the radial direction. The fluid temperature is assumed to be T_i, which is approximately 0.3–0.5 T_m, where T_m is the melting temperature of the material of the pipe. The temperature at the outer surface of the pipe is assumed to be $T_\mathrm{o} < T_\mathrm{i}$, indicating a thermal gradient of $\Delta T = T_\mathrm{i} - T_\mathrm{o}$ between the inner and the outer surface of the pipe. The pipe section has an inner radius r_i and outer radius r_o; see Fig. 1. The stresses that are generated at any location of the pipe are due to the combined effect of the fluid pressure P and the thermal gradient ΔT. Thermal creep is assumed to be the primary cause of damage and, at time t, is characterized by a non-dimensional variable, $D(t)$, that lies between 0 and 1 with zero indicating no damage. The definition for $D(t)$ is derived from continuum damage mechanics principles. The creep damage growth at any location is assumed to be modelled by the Kachanov–Robotnov law [13,14], given by

$$\frac{\mathrm{d}}{\mathrm{d}t}[D(t)] = H\left[\frac{\sigma_v(t)}{1 - D(t)}\right]^q. \tag{1}$$

Here, H and q are constants that depend on the material, and $\sigma_v(t)$ essentially represents the effective stress in a material subjected to a multi-axial state of stress at the location where the growth of creep damage is being investigated. The effective stress is interchangeably termed as the von Mises stress even though the latter was originally defined as the effective stress in materials having plastic deformations without creep. $\sigma_v(t)$ is obtained as a quadratic function of σ_r, σ_θ, and σ_z which are, respectively, the radial, hoop, and axial stress components, at any time instant, the expressions of which are provided in "Appendix". At $t = 0$ when the

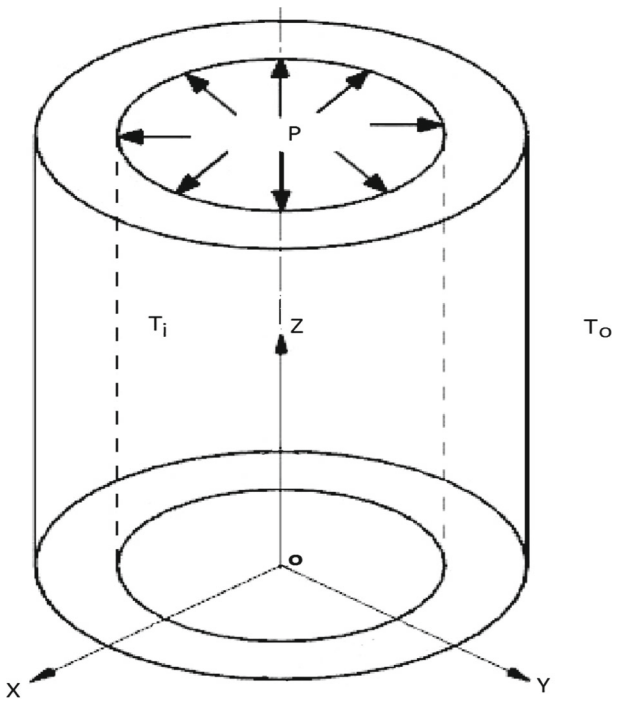

Fig. 1 Schematic diagram of the circular pipe

material is assumed to have no creep damage, the stress components are due to the combined effects of internal pressure and the thermal loads. However, with time, the effects of residual stresses due to the creep strains have contributions to the stress vector, and in turn, to the von Mises stress. The growth of the normal and shear creep strains with time is computed from the creep strain rate equations [15] and is highly nonlinear. This indicates that the creep damage growth as governed by Eq. (1) is nonlinear for which analytical solutions are not possible, and one has to resort to numerical solutions only. More details of the equations governing the growth of creep damage are available in the "Appendix".

In structural systems where the material properties have random inhomogeneities and are modelled as random fields, the components of the stress tensor have uncertain spatial variations and are random fields as well. Consequently, von Mises stress and, in turn, the thermal creep damage have random spatial variations. Moreover, on account of the nonlinearity of the creep damage growth equations, the propagation of the material uncertainties to the developed stress is nonlinear. Thus, even if the uncertainties in the material properties are modelled as Gaussian fields, the stress components are non-Gaussian whose marginal pdfs are difficult to obtain analytically. The problem is further compounded by the fact that the von Mises stress is a quadratic function of the stress components and that the creep damage at any time instant is obtained as the solution of a nonlinear differential equation. Unfortunately, Gaussian modelling of the material property random fields is not suitable as this implies a finite probability of the material parameters taking physically impossible values. As a result, non-Gaussian models for the random fields, which take strictly positive values, are more suitable. However, this makes the problem more complex and implies the need to seek numerical solutions for the thermal creep damage growth over the spatial extent of the structural system.

The focus of this study is on the development of a SFEM framework for (a) identifying the most likely regions of thermal creep failure and (b) the associated failure probability along the spatial extent of the structural system. A 3-D finite element analysis is carried out on the circular pipe section to investigate the effect of material uncertainties on damage. The material properties that are modelled as non-Gaussian fields are represented in the weak form as a series representation of a vector of correlated random variables. Subsequently, the corresponding FE equations are modified to take into account the effect of these random variables. For the sake of illustration, three cases are considered. First, only Young's modulus of elasticity is assumed to be a random field, and the most critical locations for failure are identified. In the second case, both Young's modulus of elasticity and material thermal conductivity are modelled as random fields, and the most likely regions of failure are identified. Finally, the temperature of the fluid inside the pipe is assumed to have temporal fluctuations, and hence, the boundary temperatures at the inner wall are modelled as random fields along with both the material properties considered earlier. However, before the development of the FEM formulation, the 3-D random field discretization needs to be developed. This is discussed in the following Section.

3 Optimal linear expansion

The method of optimal linear expansion (OLE) is used to represent a stationary random field $f(\boldsymbol{\mathcal{R}}, \omega)$ as a series expansion of the form [10]

$$f(\boldsymbol{\mathcal{R}}, \omega) \approx \bar{f}(\boldsymbol{\mathcal{R}}, \omega) = f_0(\boldsymbol{\mathcal{R}}) + \sum_{k=1}^{N} S_k(\boldsymbol{\mathcal{R}})\phi_k(\omega) \tag{2}$$

where $\bar{f}(\boldsymbol{\mathcal{R}}, \omega)$ is the discretized random field along the three-dimensional spatial domain $\boldsymbol{\mathcal{R}}$, N is the number of nodal points in the mesh used for the random field discretization, $f_0(\boldsymbol{\mathcal{R}}) = \langle f(\boldsymbol{\mathcal{R}}, \omega)\rangle$ denotes the ensemble mean of the process, $S_k(\boldsymbol{\mathcal{R}})$ are deterministic shape functions, $\{\phi_k(\omega)\}_{k=1}^{N}$ represents a vector of correlated random variables defined in the probability space $(\Omega, \mathcal{A}, \mathcal{P})$ associated with the N nodal points in $\boldsymbol{\mathcal{R}}$, and $\omega \in \Omega$ represents the sample space. The shape functions $S_k(\boldsymbol{\mathcal{R}})$ are determined by minimizing the variance of the error of discretization, subject to the condition that the expectation of the discretization error is zero. Mathematically, this implies that the shape functions $S_k(\boldsymbol{\mathcal{R}})$ are selected such that

$$\langle \epsilon_0(\boldsymbol{\mathcal{R}}, \omega)\rangle^2 = \left\langle \left\{ f(\boldsymbol{\mathcal{R}}, \omega) - \sum_{k=1}^{N} S_k(\boldsymbol{\mathcal{R}})\phi_k(\omega) \right\}^2 \right\rangle \tag{3}$$

is minimized where $\epsilon_0(\boldsymbol{\mathcal{R}}, \omega)$ is the discretization error, subject to the constraint $\langle \epsilon_0(\boldsymbol{\mathcal{R}}, \omega)\rangle = \langle f(\boldsymbol{\mathcal{R}}, \omega) - \bar{f}(\boldsymbol{\mathcal{R}}, \omega)\rangle = 0$. Here $\langle\cdot\rangle$ is the expectation operator and denotes the ensemble average. This leads to the set of equations

$$\mathbf{S}_k(\boldsymbol{\mathcal{R}}) = \mathbf{Q}^{-1}\mathbf{V}(\boldsymbol{\mathcal{R}}) \tag{4}$$

where $\mathbf{V}(\boldsymbol{\mathcal{R}})$ is a vector whose kth component is given by $\langle f(\boldsymbol{\mathcal{R}}, \omega) f(\boldsymbol{\mathcal{R}}_k, \omega)\rangle$ and $\mathbf{Q}$ is the covariance matrix of $f(\boldsymbol{\mathcal{R}}, \omega)$ corresponding to the nodal points whose ijth component is given by $\langle f(\boldsymbol{\mathcal{R}}_i, \omega) f(\boldsymbol{\mathcal{R}}_j, \omega)\rangle$. Here, $\boldsymbol{\mathcal{R}}_i$ denotes the ith node in the mesh used for discretizing the random field over the domain $\boldsymbol{\mathcal{R}}$. It can be shown that the shape functions have the desired property $S_k(\boldsymbol{\mathcal{R}}_j) = \delta_{jk}$, where δ_{jk} is the Kronecker delta [11]. A direct consequence of this property is that the error in discretization is zero at the nodes and hence the pdf of $f(\boldsymbol{\mathcal{R}}, \omega)$ and $\bar{f}(\boldsymbol{\mathcal{R}}, \omega)$ is identical at the nodal points. More explicit discussions on the OLE formulation are available in [10,11]. An inspection of Eq. (2) shows that the OLE representation requires only simulation of random variables corresponding to the parent distribution. Thus, the computational cost in simulating the discretized random field is significantly less than in the parent field.

One of the advantages of using OLE for random field discretization is that the mesh size depends on the correlation length of the particular random field and is distinct from the meshing used in finite element discretization. In a problem with multiple parameters modelled as random fields, one can adopt a separate random field discretization mesh for each of the fields. For the discretization of a random field in a cylindrical spatial domain, the total number of nodal points $N = m \times n \times q$ where m, n, and q indicate the number of grid points along r, θ, and z directions and N is the number of random variables used for the weak form representation of the 3-D random field. The choice of the grid size for random field discretization is dictated by minimizing the discretization error and keeping the number of random variables entering the formulation a minimum. A too coarse meshing would indicate large discretization errors and introduce additional epistemic uncertainties in the formulation, while too fine meshing would increase the number of random variables entering the formulation and increase the computational costs. In fact, it has been shown that [10]

$$\mathrm{Var}[f(\boldsymbol{\mathcal{R}}, \omega) - \bar{f}(\boldsymbol{\mathcal{R}}, \omega)] = \mathrm{Var}[f(\boldsymbol{\mathcal{R}}, \omega)] - \mathrm{Var}[\bar{f}(\boldsymbol{\mathcal{R}}, \omega)] \tag{5}$$

where $\mathrm{Var}[\cdot]$ denotes the variance. As the error variance is always larger or equal to zero, it follows that the discretized random field $\bar{f}(\boldsymbol{\mathcal{R}})$ always underestimates the variance in comparison to the original field. Therefore, there is a need to optimize the selection of N. In this study, the choice of N is selected by imposing the condition that the global mean square error is below a threshold value ϵ_1. Mathematically, this is expressed as

$$\iiint_{\boldsymbol{\mathcal{R}}} \langle \epsilon_0(\boldsymbol{\mathcal{R}})^2 \rangle \mathrm{d}\boldsymbol{\mathcal{R}} \leq \epsilon_1. \tag{6}$$

Typically, ϵ_1 is taken to be $O(10^{-4})$. For the sake of illustrating the procedure adopted for selecting the OLE mesh, we consider a 2-D rectangular spatial domain where the number of nodal points $N = m \times n$, where m and n indicate the number of grid points along the two orthogonal directions. Even for a square domain, in general $m \neq n$ unless the correlation lengths of the random field along the two orthogonal directions are equal. Assuming the correlation lengths to be equal and hence $m = n$, a plot for the global mean square error as a function of $N = n \times n$ is shown in Fig. 2. It is observed that $N = 9$, equivalent to a 3×3 grid, is sufficient.

Figure 3 shows the FE meshing, indicated by the solid line and the OLE meshing indicated by the circles. It is clear that the meshing for FE and random field discretization can be significantly different, and there is no requirement for the FE nodal points and the OLE nodal points to be coincident [12]. Figure 4 shows the contour plots for the discretization error in $\boldsymbol{\mathcal{R}}$ when a 3×3 meshing is adopted. The numbers along the contours indicate the error levels which are observed to be of $\mathcal{O}(10^{-5})$. The error is larger as the distance from the nodal points, denoted by the hollow circles, increases. The zero error contours coincide with the nodal points which are marked as hollow circles. This is clear from the error surface plot shown in Fig. 5. A similar pictorial representation for the domain of the problem considered in this paper is difficult.

For the problem considered in this paper, we assume a 3-D random field with lognormal marginal pdf, of the form

$$p(u; \mu, \sigma) = \frac{1}{s\sigma\sqrt{(2\pi)}} \exp\left[\frac{\ln u - \mu}{2\sigma^2}\right] \tag{7}$$

where $\mu = 1.38 \times 10^5$ MPa and $\sigma = 0.27 \times 10^5$ MPa. Here, u is the observed value at coordinates (x_j, y_l, z_k) in a 3-D domain. The corresponding correlation function is assumed to be of the form

$$R_{ff}(s_1, s_2, s_3) = c^2 \exp\left[-\left\{\frac{s_1^2}{c_1} + \frac{s_2^2}{c_2} + \frac{s_3^2}{c_3}\right\}\right]. \tag{8}$$

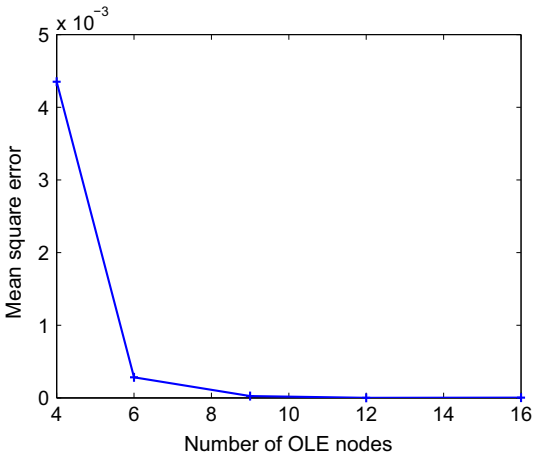

Fig. 2 Global mean square error as a function of N

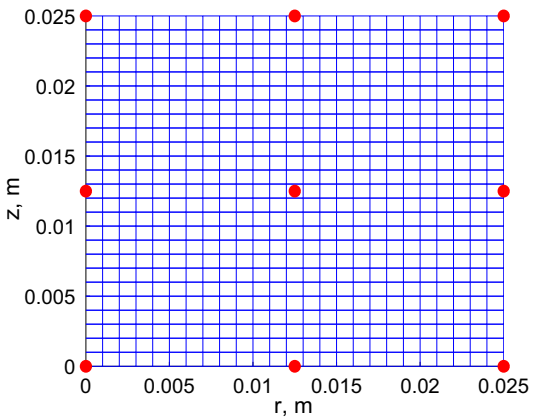

Fig. 3 Mesh grid **a** displacement fields in FE: *solid lines*, **b** random field: *circles*

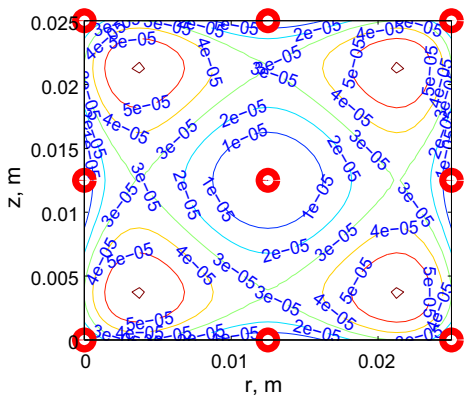

Fig. 4 Contour error plot for 2-D random field discretized with a 3×3 mesh

Here, s_1, s_2, and s_3 represent the spatial lag along x, y, and z directions, c^2 is the variance and is taken to be unity, and c_1, c_2, c_3 are correlation lengths of the field along the three x, y, and z directions. For the sake of numerical simplicity, the correlation constants are assumed to be the same in all three directions and are taken to be equal to $c_1 = c_2 = c_3 = 6$. It must be emphasized here that the choice of the model for the marginal probability density function of the field and its correlation function are for the sake of illustration; adopting

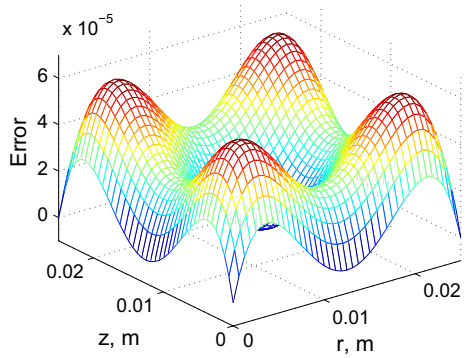

Fig. 5 Surface error plot when the 2-D random field is discretized with a 3×3 mesh

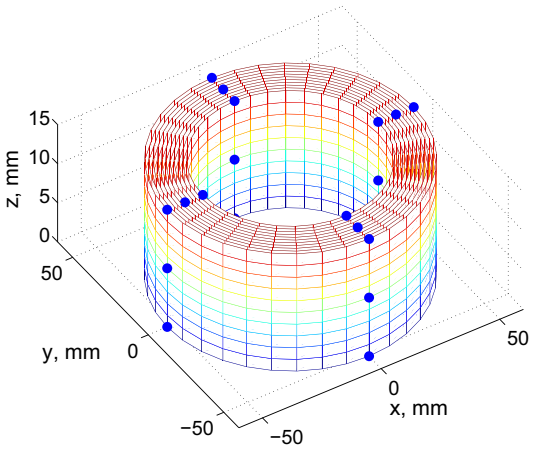

Fig. 6 Meshing: *full lines* indicate FE mesh, while the *dots* indicate OLE nodes

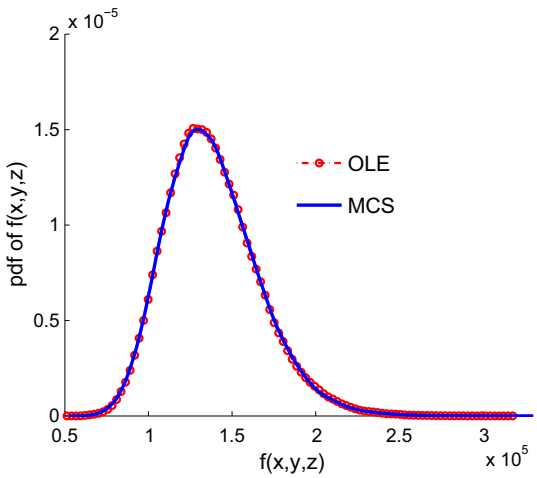

Fig. 7 Comparison of pdf of $\bar{f}(x, y, z)$ and $f(x, y, z)$ at first OLE node

alternative models does not affect the proposed methodology. For discretization of the 3-D random field, we consider a meshing with $3 \times 4 \times 3$ nodes such that $N = 36$; the corresponding global error is of $\mathcal{O}(10^{-3})$.

The mesh that is used for FE discretization is much finer. The OLE nodes, which represent physical locations on the spatial domain, are superimposed on the FE mesh shown in Fig. 6 and are shown as circles. Figure 7 shows a comparison of the pdf of the discretized field at a nodal point with the target pdf; a perfect match is

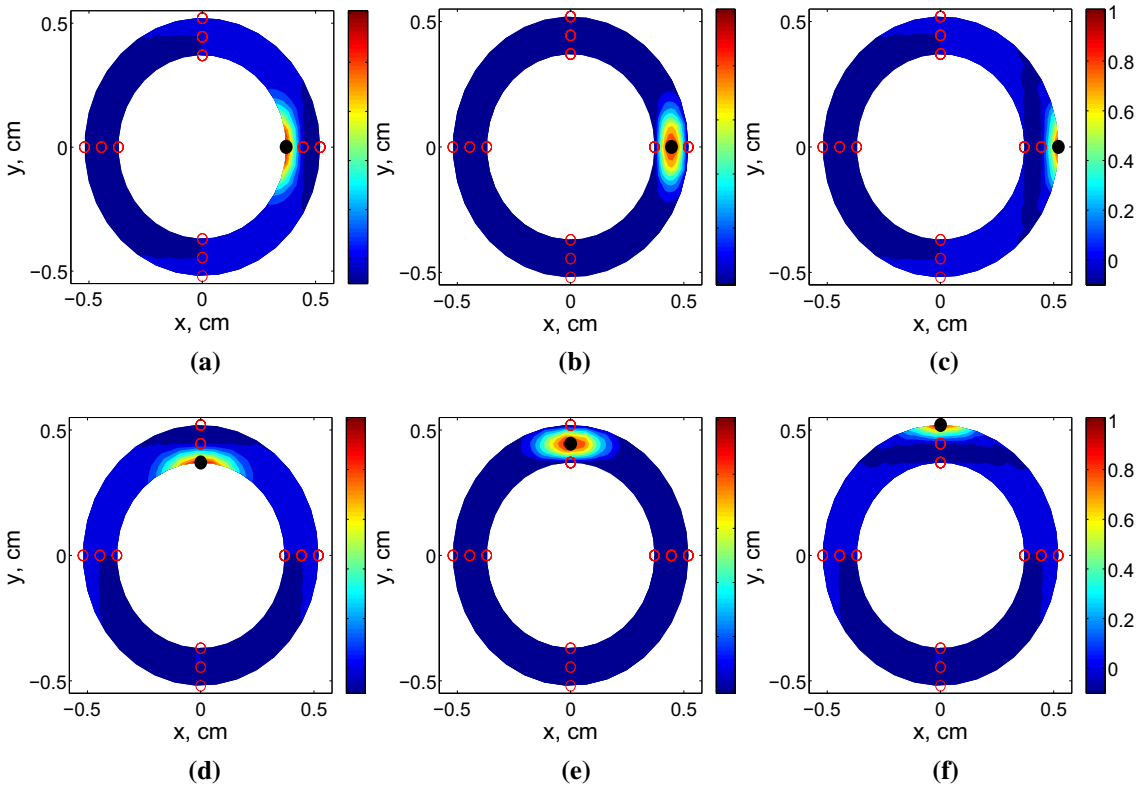

Fig. 8 2-D contours of the first six OLE shape functions at $z = z_0$; *circles* OLE nodes; contours denote the spatial variation of the numerical values of these shape functions. **a** $S_1(x, y, z = z_0)$. **b** $S_2(x, y, z = z_0)$. **c** $S_3(x, y, z = z_0)$. **d** $S_4(x, y, z = z_0)$. **e** $S_5(x, y, z = z_0)$. **f** $S_6(x, y, z = z_0)$

observed. As mentioned earlier, this follows from the property of the OLE shape functions $S_k(\boldsymbol{\mathcal{R}}_j) = \delta_{jk}$ and indicates zero error of discretization at the nodal points.

The topology of these shape functions is similar to the topology of the domain $\boldsymbol{\mathcal{R}}$, which in this case is a circular annular cylindrical pipe. Figure 8 shows the contours of the 3-D OLE shape functions corresponding to a level $z = z_0$, where the plane $z = z_0$ passes through the nodes 1–12. An inspection of these contours shows that the kth shape function $S_k(\boldsymbol{\mathcal{R}}) = 1$ at the kth node and zero at the other nodal points. It is to be noted that these shape functions take nonzero values at regions in between the nodal points implying that the discretized field may not retain the pdf characteristics of the parent field in these regions. However, as will be shown later, this does not affect the analysis as the SFEM formulation is developed based on the random field representation at the nodal points only.

4 Stochastic finite element formulation

This Section presents the formulation of the stochastic finite element framework that incorporates the effects of the random inhomogeneities in the material properties on the creep damage growth. The spatial domain considered is a section of an annular cylinder whose longitudinal dimensions are assumed to be much larger in comparison to its transverse dimensions. The FE formulation has been developed with respect to the $x - y - z$ Cartesian system. In the development of the equations, the shear deformations have been neglected. This is an assumption that has been made to simplify the problem even though the cylinder is asymmetric given the random material inhomogeneities in the material properties. Additional assumptions considered are (a) the thermal diffusivity is assumed to be infinite, and (b) the heat transfer coefficients at both the boundaries of the pipe are infinite. The implication of the second assumption is that the temperature at the boundaries of the structural component is taken to be equal to the temperature of the environment. Thus, the inner wall temperature is taken to be equal to the fluid temperature T_i, while the outer wall temperature is assumed to be that of the environment and denoted by T_o. For computing the creep damage growth as a function of time

using the equations presented in the "Appendix", the nodal stresses computed along the Cartesian coordinate system are converted in terms of the cylindrical coordinates. For the sake of simplicity of exposition, we first present the FE formulation when the material properties are modelled as deterministic. Next, the formulation is developed when only the elastic modulus is modelled as a random field. This formulation can be generalized when other properties are also treated as random fields. Additional complexities arise, however, when the thermal conductivity is also modelled as a random field, and the corresponding formulation is presented next. Finally, the case when the fluid temperature is assumed to have thermal fluctuations is addressed.

4.1 Deterministic case

First, we present a brief review of the finite element formulation for the elastic 3-D problem. The elastic strain vector at any instant t at any location in $\mathcal{R}$ is $\boldsymbol{\varepsilon} = [\varepsilon_r, \varepsilon_z, \varepsilon_\theta, \gamma_{r\theta}, \gamma_{\theta z}, \gamma_{rz}]^T$, where the first three are the normal components along the radial, longitudinal, and tangential directions, respectively, $\gamma_{r\theta}$ is the shear strain in $r-\theta$ plane, $\gamma_{\theta z}$ is the shear strain in $\theta - z$ plane, and γ_{rz} is the shear strain in the $r - z$ plane. The corresponding components in the Cartesian coordinate system are represented as $\boldsymbol{\varepsilon} = [\varepsilon_x, \varepsilon_y, \varepsilon_z, \gamma_{xy}, \gamma_{yz}, \gamma_{xz}]^T$, where the first three are the normal components along x, y and z directions, respectively, γ_{xy} is the shear strain in $x - y$ plane, γ_{yz} is the shear strain in $y - z$ plane, and γ_{xz} is the shear strain in the x-z plane. We consider the FE discretization to be carried out using eight-noded isoparametric linear hexahedral (brick) elements having three degrees-of-freedom per node, denoted by $\boldsymbol{\Delta}_e = [u, v, w]$. Here, $u \equiv u(x, y, z)$, $v \equiv v(x, y, z)$, and $w \equiv w(x, y, z)$, respectively, denote the displacements along x, y, and z directions corresponding to the Cartesian coordinates. The boundary conditions have been implemented by keeping in mind that the plane sections remain plane before and after deformations. This implies that the tangential displacement, v, has been restrained for all the nodes lying in the plane where $y = 0$, and the radial displacement, u, has been restrained for all the nodes lying in the plane $x = 0$. This condition is the same as saying that tangential displacements are zero for all nodes of the cylinder. In addition, the axial displacement, w, has been restricted for nodes at the top and bottom of the cylinder. The corresponding shape functions for the linear hexahedral (brick) element, in isoparametric form, are available in standard textbooks. The elemental stiffness matrix $\mathbf{K}_e$ is given by

$$\mathbf{K}_e = \iiint [\mathbf{B}\mathbf{C}\mathbf{B}^T] \mathrm{d}x\, \mathrm{d}y\, \mathrm{d}z \tag{9}$$

where $\mathbf{B}$ is the standard strain–displacement matrix, and $\mathbf{C} = E\mathbf{D}$ is the constitutive matrix, such that

$$\mathbf{D} = \frac{1}{(1+\upsilon)(1-2\upsilon)} \begin{pmatrix} 1-\upsilon & \upsilon & \upsilon & 0 & 0 & 0 \\ \upsilon & 1-\upsilon & \upsilon & 0 & 0 & 0 \\ \upsilon & \upsilon & 1-\upsilon & 0 & 0 & 0 \\ 0 & 0 & 0 & \left(\frac{1-2\upsilon}{2}\right) & 0 & 0 \\ 0 & 0 & 0 & 0 & \left(\frac{1-2\upsilon}{2}\right) & 0 \\ 0 & 0 & 0 & 0 & 0 & \left(\frac{1-2\upsilon}{2}\right) \end{pmatrix}. \tag{10}$$

Here, E and υ, respectively, denote the elastic modulus and Poisson's ratio. The reasons for writing the constitutive matrix in the above form will be clearer when the stochastic case is considered later in this paper.

The stress, $\boldsymbol{\sigma}$, induced due to the combined effect of pressure, temperature, and creep effect is given by

$$\boldsymbol{\sigma} = \mathbf{C}(\boldsymbol{\varepsilon} - \boldsymbol{\varepsilon}_0 - \boldsymbol{\varepsilon}_{\mathrm{cr}}) \tag{11}$$

where $\boldsymbol{\varepsilon}_0$ is the initial strain vector due to the temperature gradient and the fluid pressure, and $\boldsymbol{\varepsilon}_{\mathrm{cr}}$ is the initial creep strain (which is taken to be zero for an initially creep damage free material). The elemental force vector, $\mathbf{F}_{\mathrm{e}}$, is given by

$$\mathbf{F}_{\mathrm{e}} = \mathbf{F}_{\mathrm{p}} + \mathbf{F}_{\mathrm{t}} + \mathbf{F}_{\mathrm{cr}} \tag{12}$$

where $\mathbf{F}_{\mathrm{p}}$ is the force due to the fluid pressure $\mathbf{P}$,

$$\mathbf{F}_{\mathrm{p}} = \int_{\mathcal{S}} \left[\mathbf{N}_{\mathrm{s}}^{\mathrm{T}} \mathbf{P}\right] \mathrm{d}\mathcal{S}, \tag{13}$$

$\mathbf{F}_{\mathrm{t}}$ is the thermal contribution,

$$\mathbf{F}_{\mathrm{t}} = \iiint_{\mathcal{R}} [\mathbf{B}\mathbf{C}\boldsymbol{\varepsilon}_0] \,\mathrm{d}x\, \mathrm{d}y\, \mathrm{d}z, \tag{14}$$

and $\mathbf{F}_{\mathrm{cr}}$ is the contribution from creep,

$$\mathbf{F}_{\mathrm{cr}} = \iiint_{\mathcal{R}} [\mathbf{B}\mathbf{C}\boldsymbol{\varepsilon}_{\mathrm{cr}}] \mathrm{d}x\, \mathrm{d}y\, \mathrm{d}z. \tag{15}$$

In Eq. (13), $\mathbf{N}_{\mathrm{s}}$ is a vector that represents the boundary shape functions, and $\boldsymbol{\mathcal{S}}$ denotes the surface domain. In computing the thermal loads in Eq. (14) arising due to the thermal gradient, it is essential that the temperature at all the nodal points in the material can be calculated. The temperature at any location can be obtained from the solution of Laplace's equation, given by

$$\frac{\partial}{\partial x}\left(k\frac{\partial T}{\partial x}\right) + \frac{\partial}{\partial y}\left(k\frac{\partial T}{\partial y}\right) + \frac{\partial}{\partial z}\left(k\frac{\partial T}{\partial z}\right) = 0, \tag{16}$$

subject to the boundary conditions that the inner and outer wall temperatures are T_{i} and T_{o}, respectively. Note that if the thermal conductivity k is spatially homogenous, Eq. (16) can be simplified. However, later in this paper we consider the case where thermal conductivity is modelled as a random field, and hence, we retain the more general form of Laplace's equation.

Assembling the elemental matrices leads to the global FE equilibrium equations of the form $\mathbf{K}\Delta = \mathbf{F}$, where $\mathbf{K}$, $\mathbf{F}$, and $\boldsymbol{\Delta}$ are, respectively, the global stiffness, force and displacement matrix/vectors. These represent a set of coupled algebraic equations, the solutions of which lead to the displacements at the nodal points. Subsequently, the developed stresses for each Gauss point inside an element are computed using a standard procedure by multiplying the elemental displacement vector with the strain–displacement matrix and the constitutive matrix. Note that in displacement-based FEM, as has been adopted in this study, the displacements are continuous across the nodes but stress being derived quantities are discontinuous across elements. A least square method is adopted to transfer the stresses components from the Gauss points to the element nodes. Once the stress components are calculated at all the nodes at t_nth time instant, the creep damage and the creep strain components are computed for the t_{n+1}th time instant from the creep damage growth equations outlined in the "Appendix". These equations depend on the local values of stress components which make it possible to solve for the creep strain components and damage at all the nodes.

4.2 Case 1: Random spatial variations in the modulus of elasticity

The FE formulation discussed in the previous Section is now modified to take into account the random spatial variation in the modulus of elasticity. Here, E is modelled as a 3-D random field of the form $E(x, y, z, \omega) = \bar{E}[1 + g(x, y, z, \omega)]$, where $\bar{E}$ is the mean value about which the random fluctuations occur, and $g(x, y, z, \omega)$ is assumed to be a stationary non-Gaussian 3-D random field. Using OLE, the weak form for the random field $E(x, y, z, \omega)$ can be expressed as

$$E(x, y, z, \omega) \approx \bar{E}\left[1 + \sum_{k=1}^{N} S_k(x, y, z)\phi_k(\omega)\right] \tag{17}$$

where $\{S_k(x, y, z)\}$ and $\{\phi_k(\omega)\}$ have the same meaning as in Sect. 3. Since the modulus of elasticity is now assumed to have spatial variations, the constitutive matrix $\mathbf{C}(x, y, z, \omega) = E(x, y, z, \omega)\mathbf{D}$ is also spatially varying with each of its elements being random fields. Expressing the random variations in the elastic modulus in the additive form as shown in Eq. (17), the constitutive matrix can be expressed in the additive form as

$$\mathbf{C}(x, y, z, \omega) = \bar{E}\mathbf{D}\left[1 + \sum_{k=1}^{N} S_k(x, y, z)\phi_k(\omega)\right] = \mathbf{C}_{\mathrm{d}} + \mathbf{C}_{\mathrm{s}}(x, y, z, \omega) \tag{18}$$

where $\mathbf{C}_{\mathrm{d}}$ is identical to the constitutive matrix for the deterministic problem and represents the deterministic component while $\mathbf{C}_{\mathrm{s}}$ is the stochastic component which models the random variations. Substituting the expression for $\mathbf{C}(x, y, z, \omega)$ in Eq. (9) leads to the elemental stiffness matrix which is also expressed in the additive form as $\mathbf{K}_e(\omega) = \mathbf{K}_e^d + \mathbf{K}_e^s(\omega)$, where $\mathbf{K}_e^d$ is the deterministic component of the elemental stiffness matrix

and is identical to Eq. (9) with $\mathbf{C} \equiv \mathbf{C}_d$, while $\mathbf{K}_e^s(\omega)$ represents the stochastic components of the elemental stiffness matrix and is given by

$$\mathbf{K_e}^s(\omega) = \sum_{k=1}^{N} \iiint \bar{E} \left[\mathbf{BDB}^{\mathrm{T}}\right] S_k(x, y, z)\phi_k(\omega)\, \mathrm{d}x\, \mathrm{d}y\, \mathrm{d}z. \tag{19}$$

Note that the $\{\phi_k(\omega)\}$ in the above equation constitute a vector of correlated random variables corresponding to the nodal points for the discretized random field.

An inspection of Eqs. (12–15) reveals that the spatial random variation of the elastic modulus implies a modification in the computation of the elemental load vector as well. Here, $\mathbf{F}_{\mathrm{t}}$ and $\mathbf{F}_{\mathrm{cr}}$ are seen to be dependent on elastic modulus and hence will have deterministic as well as stochastic components. The deterministic components for thermal and creep loads are, respectively, denoted by $\mathbf{F}_{\mathrm{t}}^d$ and $\mathbf{F}_{\mathrm{cr}}^d$ and are identical to the expressions given in Eqs. (14) and (15). The expressions for their corresponding stochastic components, $\mathbf{F}_{\mathrm{t}}^s$ and $\mathbf{F}_{\mathrm{cr}}^s$, are given by

$$\mathbf{F}_{\mathrm{t}}^s(\omega) = \sum_{k=1}^{N} \iiint_{\mathcal{R}} [\bar{E}\mathbf{BD}\boldsymbol{\varepsilon}_0] S_k(x, y, z)\phi_k(\omega)\mathrm{d}x\, \mathrm{d}y\, \mathrm{d}z \tag{20}$$

and

$$\mathbf{F}_{\mathrm{cr}}^s(\omega) = \sum_{k=1}^{N} \iiint_{\mathcal{R}} [\bar{E}\mathbf{BD}\boldsymbol{\varepsilon}_{cr}] S_k(x, y, z)\phi_k(\omega)\mathrm{d}x\, \mathrm{d}y\, \mathrm{d}z. \tag{21}$$

The expressions for $\boldsymbol{\varepsilon}_0$ and $\boldsymbol{\varepsilon}_{cr}$ are available in the "Appendix". The left-hand side of the three-dimensional integrals in Eqs. (19–21) as well as the integrands consist of matrices/vectors. These expressions are to be interpreted to be the generic form for computing the elements of matrices/vectors in the left-hand side of these equations. It is to be noted that the integrands consist of the vector of correlated random variables $\{\phi_k(\omega)\}$, and hence, the elements of the $\mathbf{K}_e^s$, $\mathbf{F}_{\mathrm{t}}^s$, and $\mathbf{F}_{\mathrm{cr}}^s$ are functions of these random variables.

Following the formulation discussed in this Section, first an ensemble of correlated random variables $\{\phi_k(\omega)\}$ having the desired marginal pdf and correlation characteristics is simulated using Monte Carlo simulations (MCS). Subsequently, realizations for the stochastic components of the stiffness and the load vectors are numerically computed based on the formulation presented in this Section. As the shape functions $\{S_k(x, y, z)\}$ are available numerically, the evaluation of the three-dimensional integrals in Eqs. (19–21) is carried out numerically using Gauss' quadrature scheme. The damage trajectories with time are subsequently computed corresponding to each realization. This is discussed in more details later in the paper. In the next Section, discussions on the additional complexities that arise in the formulation are presented when the material thermal conductivity is also assumed to have spatial random fluctuations.

4.3 Case 2: Random spatial variation in the modulus of elasticity and thermal conductivity

Random spatial variations in the material properties such as thermal conductivity can be incorporated into the analysis following an identical procedure as has been discussed in the previous Section. For each material property modelled as a random field, one would require a different meshing based on the correlation length for the particular field, which in turn will introduce an additional vector of correlated random variables. The primary difficulty that arises in the formulation when the thermal conductivity is modelled as a random field is the inability to obtain an analytical solution of the Laplace equation given in Eq. (16), to compute the temperature at all the nodal points in the FE discretized model. This presents a difficulty in obtaining the force vector $\mathbf{F}_t$. To bypass this difficulty, the temperature at the nodal values has to be computed using SFEM as well. As a first step, the 3-D random field for thermal conductivity, $k(x, y, z)$, is expressed using OLE as

$$k(x, y, z, \omega) = \bar{k}\left[1 + \sum_{n=1}^{M} \psi_n(x, y, z)\zeta_n(\omega)\right] \tag{22}$$

where $\bar{k}$ is the mean value of the thermal conductivity, $\psi_n(x, y, z)$ are the OLE shape functions, and $\{\zeta_n(\omega)\}_{n=1}^{M}$ is the vector of correlated random variables associated with M nodal points. The weak form representation for the random field modelling for the elastic modulus is given in Eq. (17). As discussed in Sect. 3, the number of

terms in the OLE representation of a random field depends on the correlation length of the field, and therefore, in general, $N \neq M$.

The OLE representation for thermal conductivity $k(x, y, z, \omega)$, as given in Eq. (22), is substituted in Eq. (16), and a weak form of the Laplace equation for an element is obtained as $\mathbf{R}_e^T \mathbf{T}_e = \mathbf{0}$, where $\mathbf{T}_e$ represents the vector of temperature at the nodes of an element, $\mathbf{R}_e$ is a square matrix obtained from the weak form representation of Eq. (16). Since the thermal conductivity is expressed in an additive form, $\mathbf{R}_e(\omega) = \mathbf{R}_e^d + \mathbf{R}_e^s(\omega)$, where

$$\mathbf{R}_e^{d^T} = \iiint \bar{k} \left[\mathbf{B}_t \mathbf{B}_t^T \right] \mathrm{d}x \, \mathrm{d}y \, \mathrm{d}z, \tag{23}$$

$$\mathbf{R}_e^{s^T}(\omega) = \iiint \sum_{n=1}^{M} \psi_n(x, y, z) \zeta_n(\omega) \left[\mathbf{B}_t \mathbf{B}_t^T \right] \mathrm{d}x \, \mathrm{d}y \, \mathrm{d}z. \tag{24}$$

Here, $\mathbf{B}_t$ is distinct from the strain–displacement matrix $\mathbf{B}$ used earlier and is given by

$$\mathbf{B}_t = \begin{bmatrix} \frac{\partial N_1}{\partial x} & \frac{\partial N_2}{\partial x} & \frac{\partial N_3}{\partial x} & \frac{\partial N_4}{\partial x} & \frac{\partial N_5}{\partial x} & \frac{\partial N_6}{\partial x} & \frac{\partial N_7}{\partial x} & \frac{\partial N_8}{\partial x} \\ \frac{\partial N_1}{\partial y} & \frac{\partial N_2}{\partial y} & \frac{\partial N_3}{\partial y} & \frac{\partial N_4}{\partial y} & \frac{\partial N_5}{\partial y} & \frac{\partial N_6}{\partial y} & \frac{\partial N_7}{\partial y} & \frac{\partial N_8}{\partial y} \\ \frac{\partial N_1}{\partial z} & \frac{\partial N_2}{\partial z} & \frac{\partial N_3}{\partial z} & \frac{\partial N_4}{\partial z} & \frac{\partial N_5}{\partial z} & \frac{\partial N_6}{\partial z} & \frac{\partial N_7}{\partial z} & \frac{\partial N_8}{\partial z} \end{bmatrix} \tag{25}$$

where $\{N_i\}_{i=1}^8$ are the standard FE shape functions corresponding to the eight-noded linear hexahedral elements that have been used for FE discretization. Assembling the global matrices leads to the system of equations

$$\mathbf{R}^T(\omega)\mathbf{T} = \mathbf{0} \tag{26}$$

where $\mathbf{T}$ is the global vector of the nodal temperatures in the spatial domain of the structure. As the temperature at the nodal points in the inner and the outer surfaces of the pipe is known, the above system of equations can be solved for each realization of the random vector $\{\zeta_n(\omega)\}$. Once the temperature at all the nodal points is computed, the temperature gradient and, in turn, the initial strain due to $\boldsymbol{\varepsilon}_0$ at these nodes can be calculated. Subsequently, the force vector due to the thermal gradients, $\mathbf{F}_\mathrm{t}$, is computed from Eq. (20). The effect of the spatial randomness in the elastic modulus of the material is addressed using the formulation discussed in the previous Section. Note that in computing the force vector $\mathbf{F}_\mathrm{t}$, the effects of spatial randomness in the elastic modulus are through the constitutive matrix $\mathbf{C}$ while the effect of the spatial randomness in the thermal conductivity are through the initial strain vector $\boldsymbol{\varepsilon}_0$. Thus, $\mathbf{F}_\mathrm{t}$ is a function of the random variables $\{\zeta_n(\omega)\}$ and $\{\psi_k(\omega)\}$.

4.4 Case 3: Random temporal variations in fluid temperature and random spatial variations in the material properties

We next generalize the proposed method to incorporate into the analysis the effects of random temporal fluctuations in the fluid temperature. We assume that the inner wall of the structural component and the fluid temperature are equal at all time instants. We model the random spatial variations in the material properties—modulus of elasticity and thermal conductivity—using OLE as discussed in the earlier Sections. In case 2, the boundary nodal temperatures for each element are computed for each time instant and for each realization based on the deterministic input values of the inner and outer boundary temperatures. However, in this case, the boundary temperatures for inner surface, i.e. T_i, are assumed to be fluctuating about a mean value, and T_o is assumed to be constant. We model T_i as a stationary Gaussian random process with mean value $\bar{T}_i$ and represent it as a Karhunen–Loève (KL) expansion, having the form

$$T_\mathrm{i}(t, \omega) = \bar{T}_\mathrm{i} + \sum_{j=1}^{\infty} c_j(\omega) \psi_j(t). \tag{27}$$

Here, $\bar{T}_\mathrm{i}$ is the mean temperature about which the fluctuations occur, $c_j(\omega)$ are zero mean independent random variables having variance λ_j, and $\psi_j(t)$ and λ_j are, respectively, the eigenvectors and the corresponding eigenvalues obtained by solving the integral equation

$$\int_{\mathcal{D}} R_{TT}(t, s) \psi_j(s) \mathrm{d}s = \lambda_j \psi_j(t). \tag{28}$$

Note that $R_{TT}(t, s)$ is the autocovariance function of the random process $T_{\mathrm{i}}(t, \omega)$. It is worth mentioning here that $T_{\mathrm{i}}(t, \omega)$ could be discretized using OLE as well. Instead KL expansion has been used for the weak form representation of $T_{\mathrm{i}}(t, \omega)$ as (a) it is modelled as a 1-D Gaussian process for which KL expansions are simpler and (b) KL expansions have been shown to be optimal spectral representations, implying that the weak form representation requires the least number of random variables.

The implication of having temporal fluctuating temperatures implies that the boundary nodal temperatures for each element will change at each instant of time. Subsequently, the temperature at the FE nodal points needs to be computed, at each time instant, by solving the Laplace equation. Note that a solution of the Laplace equation is obtained in the weak form using the procedure discussed in the earlier Section. The rest of the analysis remains the same as in Case 2. A more complicated analysis that takes into account the transport of fluid through the pipe and the temporal and spatial variations of the heat transfer is beyond the scope of this study.

5 Failure probability

The creep damage growth equations outlined in the "Appendix" reveal that the local creep damage at any instant of time depends on the local material properties and the temperature gradient. In structural systems with random spatial inhomogeneities, it is obvious that the creep damage at any instant of time has spatial variations whose characteristics depend on the underlying properties of the spatial random inhomogeneities in the modulus of elasticity and thermal conductivity. Hence, the creep damage itself is a random field whose probabilistic characteristics are not obvious, given the nonlinear nature of the creep damage growth. Moreover, if a failure is defined to occur when the creep damage at any location exceeds a specified value, the spatial location where the failure originates can be characterized only in the probabilistic sense.

The SFEM formulation presented in this paper enables a numerical approach for analysing the growth of creep damage over the spatial extent of the component and characterizing in a probabilistic sense the creep damage spatial variation at any instant of time. Moreover, we can estimate the failure probability at specified locations and, in turn, identify the most likely failure regions. This involves the following steps:

1. Using standard Monte Carlo simulation methods, simulate an ensemble for the vectors of correlated random variables $\{\psi(\omega)\}$ and $\{\zeta(\omega)\}$. Assume the ensemble is of size Z.
2. Construct the FE matrices corresponding to each realization of the random variables. Solve for the creep damage growth at all the nodal points within the spatial extent of the structure in an iterative manner, for time $[t_0, t_f]$, where t_0 is initial time taken to be zero and t_f is final time. If D exceeds the critical threshold D_c at time $t < t_f$, the computations are terminated for the particular realization of the random variables. Store all the results.
3. Repeat the previous step for all Z realizations of the random variables.
4. Statistically process the ensemble of results obtained from the previous steps to obtain probabilistic descriptors for the failure probability associated with all the nodal points.

The mathematical statement for the computation of the failure probability in terms of creep damage, at any time instant t, is given by

$$P_f = \int_{D_c}^{\infty} p_D(s; t)\ \mathrm{d}s = 1 - P[D(t) \leq D_c] = 1 - P_D(D_c; t). \tag{29}$$

Here, $D(t)$ is the creep damage at time instant t, at a particular location, $P[\,\cdot\,]$ is probability measure, and $p_D(\cdot)$ is the probability density function of D at time t at that location. Clearly, $p_D(\cdot)$ changes with t, indicating the non-stationary nature of the growth of stochastic creep damage. Computation of the failure probability at all the nodes of the structure helps to identify the location in the structure which has the highest probability density function for the failure probability and is useful in identifying the most likely regions from where failure due to creep originates.

6 OLE representation of the random field from measurement data

A primary requirement in the proposed methodology is the knowledge of the second-order characteristics of the random fields used in modelling the material inhomogeneities. However, in practical situations, only

the data from sample measurements are available. Of course, one can carry out a statistical analysis and fit a second-order probabilistic model that is consistent with the data. This implies that one needs to estimate the marginal probability density function and the correlation function from the available measurements, which is discussed next.

Consider a random field $f(\boldsymbol{\mathcal{R}}, \omega)$ defined in an spatial domain $\boldsymbol{\mathcal{R}}$ to be represented by an N-dimensional random vector $\mathcal{F} = [f_1, \ldots, f_N]^T$, where f_j represents the random variable $f(\boldsymbol{\mathcal{R}} = \boldsymbol{\mathcal{R}}_j)$. Let $P_{\mathcal{F}} = P_{f_1 \ldots f_N}$ be the corresponding joint probability density function. As is well known, a complete characterization of the random field $f(\boldsymbol{\mathcal{R}}, \omega)$ in terms of the discrete form requires the information of $P_{\mathcal{F}}$ when $N \to \infty$. This is, however, impractical, and therefore, the probabilistic characterization of $f(\boldsymbol{\mathcal{R}}, \omega)$ by the probabilistic descriptors of $\mathcal{F}$ is always approximate.

The data from field measurements can be considered as a sample realization of $\mathcal{F}$. The crux lies in obtaining an OLE representation for the stochastic field $\mathcal{F}$, which is an approximation of the random field $f(\boldsymbol{\mathcal{R}}, \omega)$, using the measurement data such that the joint probability density function of $\mathcal{F}$ and $f(\boldsymbol{\mathcal{R}}, \omega)$ is equivalent. Here, we use the fact that the components of $\mathcal{F}$ denoted by $\mathbf{f}_j$ are random variables and their OLE representation at $\boldsymbol{\mathcal{R}} = \boldsymbol{\mathcal{R}}_j$ can be expressed as

$$\mathbf{f}_j = f(\boldsymbol{\mathcal{R}}_j, \omega) = f_0(\boldsymbol{\mathcal{R}}_j) + \sum_{k=1}^{N} S_k(\boldsymbol{\mathcal{R}}_j)\phi_k(\omega). \tag{30}$$

As has been shown earlier, $S_k(\boldsymbol{\mathcal{R}}_j) = \delta_{jk}$ and implies that $\mathbf{f}_j = f_0(\boldsymbol{\mathcal{R}}_j) + \phi_k(\omega)$. In the absence of a continuous function for the covariance of the field, the crux lies in estimating the shape functions $S_k(\boldsymbol{\mathcal{R}})$ from the measurement data. Clearly, the shape functions can be estimated in numerical form $S_k(\boldsymbol{\mathcal{R}}) = [S_k(\boldsymbol{\mathcal{R}}_1), \ldots, S_k(\boldsymbol{\mathcal{R}}_N)]$. This is obtained by constructing the $N \times N$ covariance matrix from the measurement data, sampled at N discrete points, as well as numerically computing $\mathbf{V}$ in Eq. (4). Thus, the steps involved in obtaining OLE representation of a random field from measurement data are as follows:

1. Take measurements and collect the sample realizations of the random field $\mathcal{F}$ which is an approximation of the continuous random field $f(\boldsymbol{\mathcal{R}}, \omega)$.
2. Construct the marginal pdf of the components of $\mathbf{f}_j \in \mathcal{F}$ from the normalized histogram of the sample realizations of $\mathbf{f}_j$, for all $j = 1, \ldots, N$.
3. Construct the covariance matrix from the measurement data for all the components of $\mathcal{F}$. This is $\mathbf{Q}$ used in Eq. (4).
4. Using Eq. (4), one can construct the OLE representation of the random fields.
5. Samples of $\phi_k(\omega)$ are simulated using standard simulation algorithms and used in conjunction with Eq. (30) to obtain approximations for the continuous random fields $f(\boldsymbol{\mathcal{R}}, \omega)$ in the method proposed in this paper.

Note that in the numerical calculations presented later, in the absence of availability of measurement data assumptions were made about the second-order characteristics of the random fields directly.

7 Numerical example and discussion

The formulation presented in this paper is next demonstrated by a numerical example. A section of a pipe carrying high-temperature fluid, as shown in Fig. 1, is considered. The inner and the outer radii of the pipe are taken to be $r_\mathrm{i} = 0.037$ m and $r_\mathrm{o} = 0.052$ m. The pipe dimensions along the longitudinal direction are assumed to be significantly larger than the cross-sectional dimensions. The internal fluid pressure exerted on the pipe is assumed to be $P = 3.43$ MPa. The material for the pipe is taken as HK40. The numerical values of the material and damage parameters are taken from the literature [16] and are as follows: modulus of elasticity $\bar{E} = 1.38 \times 10^5$ MPa, Poisson's ratio $\nu = 0.31$ thermal conductivity $k = 293$ W/mK, coefficient of thermal expansion $\alpha = 1.5 \times 10^{-5}(1/^\circ\mathrm{C})$, creep damage parameters $A = 1 \times 10^{-38.713}$, $n = 6.91$, $H = 1 \times 10^{-24.787}$ and $q = 6.6473$, respectively. The effective stress $\psi(\sigma)$ is taken to be equal to the von Mises stress, σ_v. The material is assumed to be defect free initially, i.e. $D_{c_0} = 0$, and all the creep strain components are zero at $t = 0$. The method for solution we have outlined in Sect. 4 is only applicable till $D_{c_0} < 1$.

The inner wall temperature of the pipe is assumed to be $T_\mathrm{i} = 800\,^\circ\mathrm{C}$, and the external wall temperature is taken to be $T_\mathrm{o} = 720\,^\circ\mathrm{C}$. For case 3, where the temperature at the inner wall is assumed to have temporal fluctuations, the temperature is modelled as a stationary Gaussian random process in time having mean value

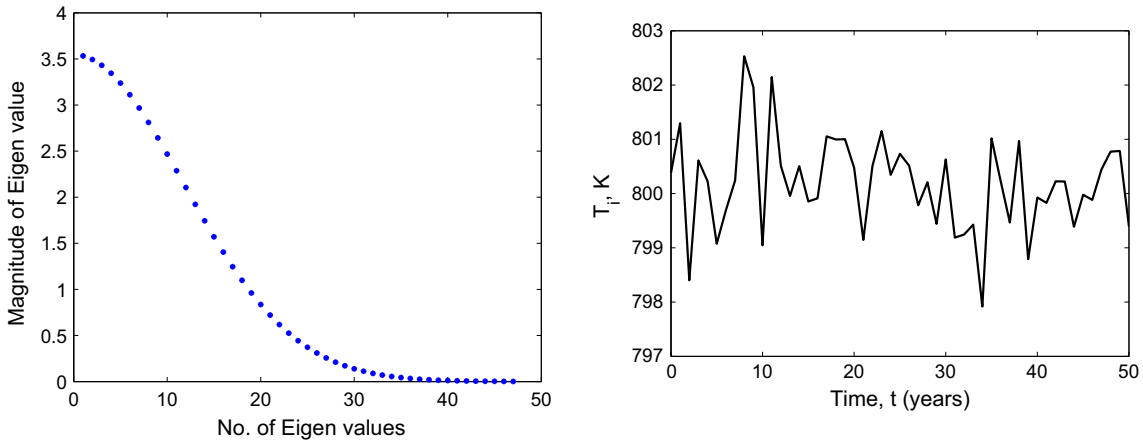

Fig. 9 KL representation of the stochastic process for the temporal temperature fluctuations: **a** magnitude of the first 50 eigenvalues and **b** a realization of a time history for the temporal fluctuations

of 800 °C, and autocovariance function of the form $R_{T_i T_i}(t) = \sigma_1^2 e^{-\alpha_1 t^2}$. The numerical values considered here are $\sigma_1 = 1$ and $\alpha_1 = 0.25$. The time interval of interest $t_f - t_0$ is assumed to be 50 years. Hence, in the numerical simulation, time histories for T_i are simulated for 50 years with the time increments taken to be $\mathrm{d}t = 0.5$ years. Note that the creep damage evolution takes place at long time scales, and hence the time increments are in the order of years. For a KL representation of the process, the integral eigenvalue problem in Eq. (28) is solved numerically. The number of terms in the KL expansion depends on the total number of eigenvalues obtained which in turn depends on the resolution of the representation of the kernel function. However, the KL expansion can be represented using a smaller subset of the basis functions defined by the eigenfunctions, and the number of terms to be retained can be estimated based on a tolerance level. It can be shown that the number of terms n to be retained depends on the condition $\sum_i^n |\lambda_i| < \epsilon_{\mathrm{tol}}$, where ϵ_{tol} is an error tolerance. Assuming $\epsilon_{\mathrm{tol}} = 1 \times 10^{-3}$, it turns out that $n = 47$. Figure 9a shows the relative magnitude of the first 50 eigenvalues λ_i. A typical time history for the inner wall temperature obtained using KL expansion with $k = 47$ terms is plotted as shown in Fig. 9b.

The pipe section is first discretized using finite elements. The FE mesh geometry of the 3-D domain is discretized using a $10 \times 36 \times 10$ grid, with 10 being the number of divisions along the radial and axial directions, and 36 is the number of divisions along the tangential direction. As mentioned earlier, linear hexahedral 3-D brick elements have been used for the FE discretization, having 8 nodes. Each node is assumed to have three degrees-of-freedom corresponding to displacements along the local Cartesian coordinate axes. A total of 3600 elements have been used in the analysis. The total number of nodes is 4356 with the active degrees-of-freedom being equal to about 13,000. Note that the axial deformations on all the nodes on the top and bottom surfaces have been restrained.

The input random field variations for the elastic modulus and thermal conductivity have been obtained using log normal distribution, whose general form is given by Eq. (7), and the autocovariance function is assumed to be of the form given in Eq. (8). The numerical values for the parameters for the two fields are given in Table 1. Figure 10 shows the spatial variation in the modulus of elasticity for a sample realization of the random field, while Fig. 11 shows the spatial variation of thermal conductivity for a sample realization of the corresponding random field.

The steps involved using the proposed method (hereafter referred to as **Method 1**) are as follows:

1. An ensemble of Z realizations of elemental stiffness matrices $\mathbf{K_e}$ is simulated.

Table 1 Parameters for the random fields for the material properties

Property	μ	σ	c_1	c_2	c_3
E	1.38×10^5 MPa	0.276×10^5 MPa	0.06	0.06	0.06
k	273 W/mK	54.6 W/mK	0.06	0.06	0.06

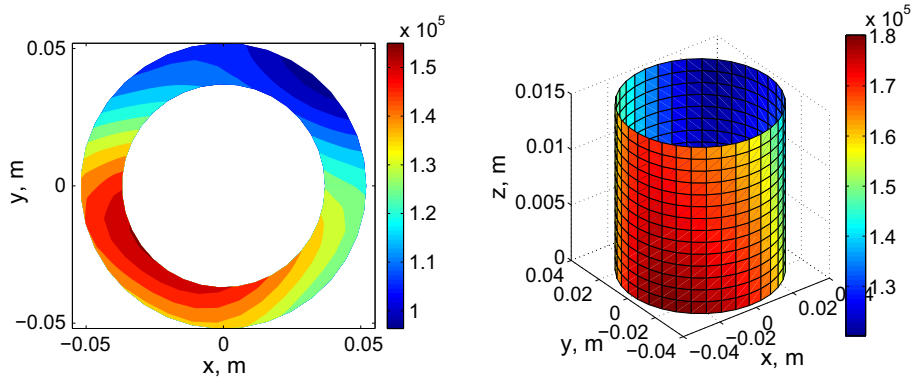

Fig. 10 Sample realization of the random field for Young's modulus of elasticity E. **a** Contours for the variation at $z = 0$. **b** The variation at the inner wall

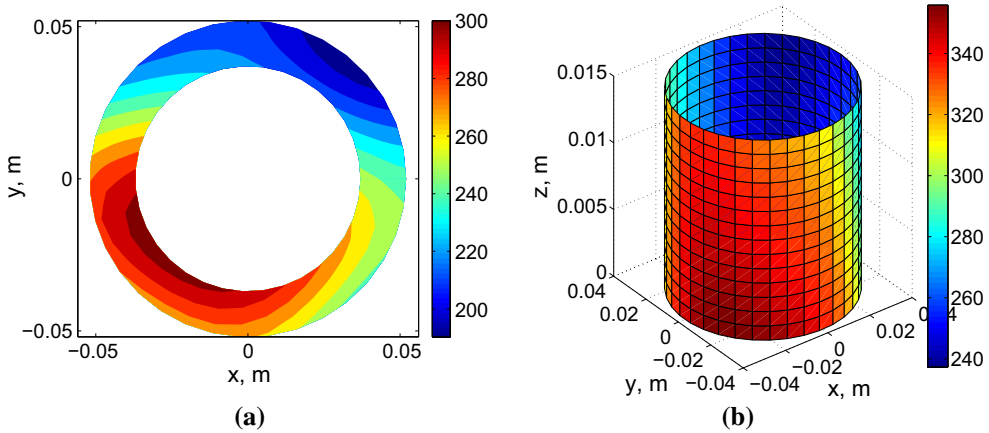

Fig. 11 Sample realization of the random field for thermal conductivity k. **a** Contours for the variation at $z = 0$. **b** The variation at the inner wall

2. Following the formulation developed in Sect. 4, the global stiffness matrix **K** is constructed numerically.
3. Corresponding to each realization of Z_i , the FE equations are solved deterministically, and the creep strains are calculated at all the Gauss points, and subsequently, the values at the nodal points are interpolated.
4. The failure probability of damage at each of the nodal points is computed from statistical processing of the results obtained from the Z realizations.

The following Sections present results obtained using Method 1.

7.1 von Mises stress

At $t = 0$, it is assumed that the initial creep strains are zero, and hence, the stress components are due to the effects of the thermal gradient and internal fluid pressure only. The von Mises stress is computed at all the nodal points at $t = 0$ for the three cases mentioned in the previous Section. Figure 12 shows a sample realization of the spatial variation of the von Mises stress for the three cases at the inner wall, where the developed stress is maximum.

7.2 Creep damage

The FE discretized equations are now numerically integrated in the time domain to obtain the creep damage growth at all the nodal points within the domain of the circular pipe section. The effects of uncertainties in the

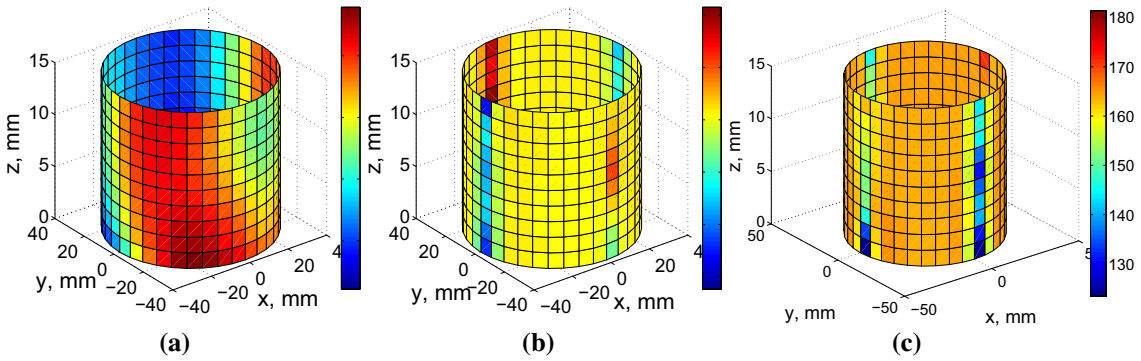

Fig. 12 Spatial variation of the von Mises stress for a sample realization; **a**–**c** shows variation along the inner wall. **a** Case 1. **b** Case 2. **c** Case 3

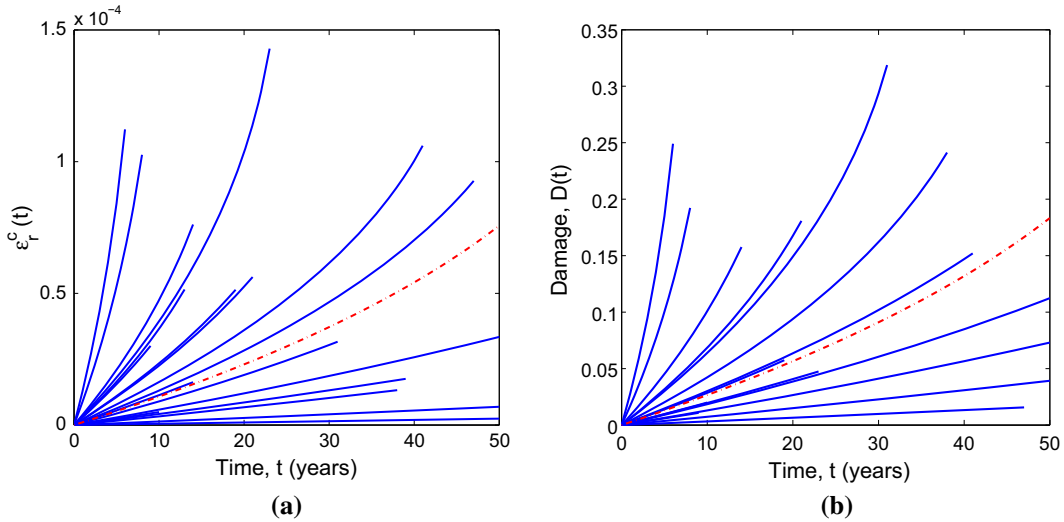

Fig. 13 Growth trajectories of **a** radial creep strain and **b** thermal creep damage; *dashed line* deterministic system; *full lines* Case 1

material properties are incorporated into the FE analysis through the vector of random variables appearing in the OLE representation. These correlated random variables are simulated using MCS, and the damage growth corresponding to each realization is computed based on the creep damage growth equations mentioned in the "Appendix". The analysis carried out in the previous Section has established that the most critical location in the domain lies on the inner wall boundary. Figure 13a shows the sample trajectories for creep strain in r-direction for the nodal point corresponding to the inner wall boundary, while Fig. 13b shows the corresponding damage growth trajectories. Here, the dotted line corresponds to the deterministic case, while the solid lines represent sample damage growth trajectories for Case 1. An inspection of these Figures reveals that a significant scatter is observed in the thermal creep strain and thermal creep damage at a given time instant. This observation is qualitatively corroborated from the scatter observed in experimental observations [1] and highlights the importance of appropriately modelling the spatial inhomogeneities in the material properties. Moreover, it is observed that the scatter grows in time. This can be explained by the fact that the uncertainties accumulate with time.

We next investigate how the growth in creep damage progresses with time over the entire cylindrical spatial domain. Figure 14 shows the spatial variation of thermal creep damage at $t = 35$ years for Cases 1, 2, and 3. Unlike the deterministic case, we observe that the creep damage growth is spatially inhomogeneous, which can be attributed to the local effects arising due to the variations in the material properties and is expected to be different for each realization of the fields. The spatial variation of the mean damage at $t = 20$ years along the inner wall is shown in Fig. 15. The spatial variability in the mean creep damage observed at the inner wall highlights the importance of taking into account the spatial random inhomogeneities. Importantly,

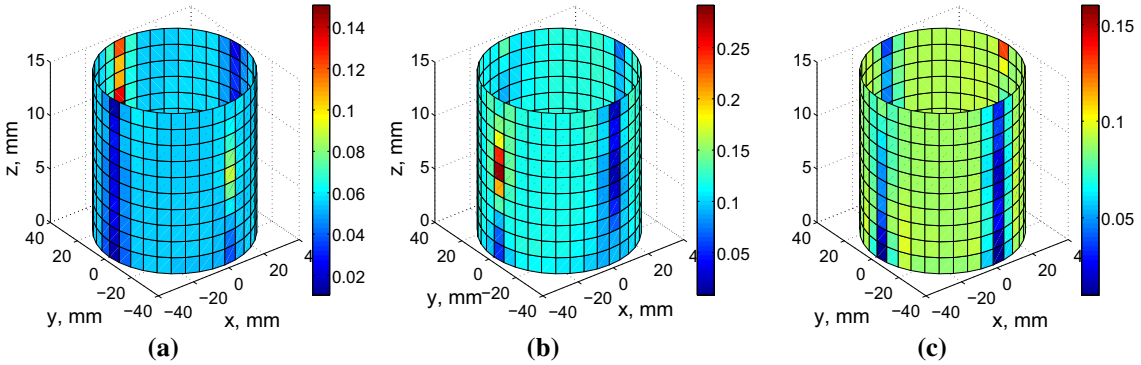

Fig. 14 Spatial variation of thermal creep damage at $t = 35$ years for a sample realization. **a** Case 1. **b** Case 2. **c** Case 3

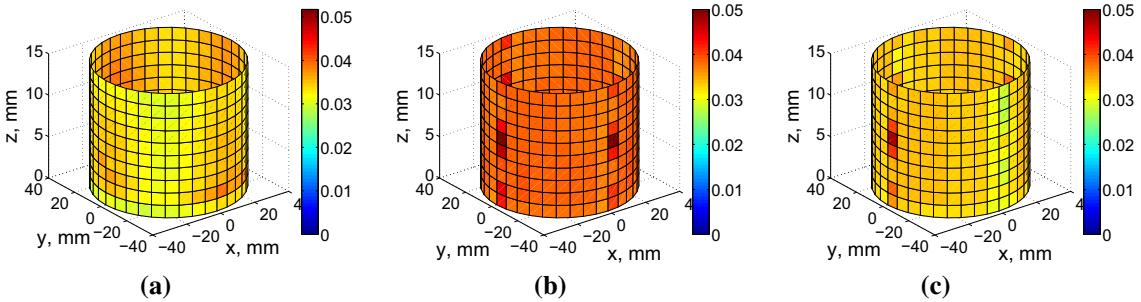

Fig. 15 Spatial variation of the mean creep damage at $t = 20$ years; **a–c** denote variation along the inner wall. **a** Case 1. **b** Case 2. **c** Case 3

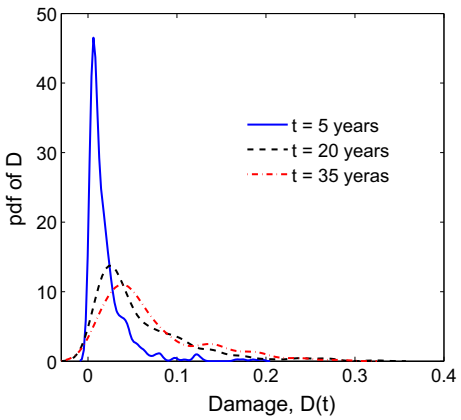

Fig. 16 Case 1: evolution of pdf of damage at a specified node

a quantitative comparison between Figs. 15a–c reveals that the creep damage is maximum in Case 2 and minimum in Case 1. The mean creep damage is less in Case 3 than in Case 2 because in Case 3 the temperature fluctuates about the mean ambient temperature considered in Case 2, and hence, the thermal loading in Case 2 is larger than in Case 3, over the same time interval. The significantly lower creep damage in Case 1 highlights that the spatial fluctuations in the thermal conductivity play a significant role in the creep damage growth. It is clear that the creep damage at any location, at any time instant, varies in each realization and is clearly a random variable. Statistical processing of the computed damage at all the nodal points enables evaluating the pdf of damage at a particular location and investigating how this propagates with time. Figure 16 shows the pdf of creep damage at a particular nodal point on the inner wall boundary of the cylinder for time instants $t = 5$, 20 and 35 years, when only the elastic modulus is assumed to be spatially random. It is clearly seen that with time the pdf becomes flatter and has a wider spread indicating its non-stationary nature. Further, it can be observed that the mean value of the pdf moves towards right indicating the growth in the damage

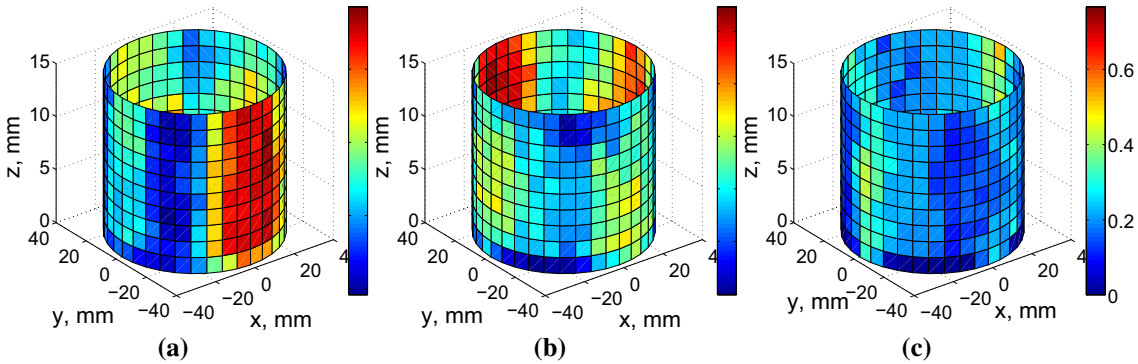

Fig. 17 Spatial variability of the failure probability at the inner wall at $t = 35$ years. **a** Case 1. **b** Case 2. **c** Case 3

with time. The higher spread in the pdf for larger time can be attributed to the historical cumulative effects of the uncertainties associated with the creep damage growth in time. A similar trend is observed in the time evolution of the pdf for creep damage when elastic modulus, thermal conductivity, and temperature loading are modelled as random fields.

7.3 Failure probability

We next focus on estimating the failure probability in terms of the creep damage. Even though the creep damage variable, D, is assumed to lie between 0 and 1 with unity indicating failure, in reality, a structural failure occurs typically when D reaches a value that lies between $0.2 - 0.3$. In this study, we define the critical threshold value $D_c = 0.1$, and a failure is deemed to occur when $D \geq D_c$. Using the results obtained from the computations carried out in the previous Sections, the creep damage at all the nodal points at different time instants is available corresponding to all the realizations of the material property random fields. An estimate of the failure probability, at a given time instant, for all the nodal points is computed from the relative frequency of the number of samples which satisfy the criterion $D \geq D_c$. Note that we consider a smaller value for D_c for the purpose of illustration so that we have at least a few sample realizations of the ensemble of Z samples which fail, and hence the relative frequency definition can be used for estimating the failure probability. Alternatively, one can obtain the pdf of the damage variable and compute the failure probability using Eq. (29). Figure 17 shows the spatial variation of the failure probability estimates for the three cases at $t = 35$ years. An inspection of these Figures clearly shows that the predictions of the failure probability at any specified location are least in Case 1, where the spatial random inhomogeneities in the thermal conductivity have not been considered. This clearly underlines the importance of spatial inhomogeneities in the thermal conductivity. Further, it is observed that the failure probability estimates in Case 3 are lower at specified locations in comparison to Case 2. This is in corroboration to the results in terms of the mean creep damage observed earlier and can be explained as the effect of thermal fluctuation about the mean value considered in Case 2, and hence, the time of exposure and in turn the thermal loadings are lower in Case 3 in comparison to Case 2.

7.4 Validation of the proposed method

In this Section, studies are carried out to investigate the performance of Method 1. To examine the accuracy of Method 1, the problems are examined using two alternative methods discussed next:

– *Method 2* As in Method 1, the spatial random fluctuations in the material properties are incorporated into the analysis by modelling them as 3-D random fields. However, no separate random field meshing is considered. Instead, once the FE meshing is carried out, the material property random fields within an element are assumed to be spatially uniform and are taken to be the representative values at the elemental centroid. Thus, the fields are now represented by a vector of correlated random variables which capture the pdf and the correlation characteristics exactly. However, the spatial variations within each element are neglected. As the FE meshing is usually much finer than the OLE random field meshing, the number of random variables entering the formulation—equal to the number of finite elements that the structure has

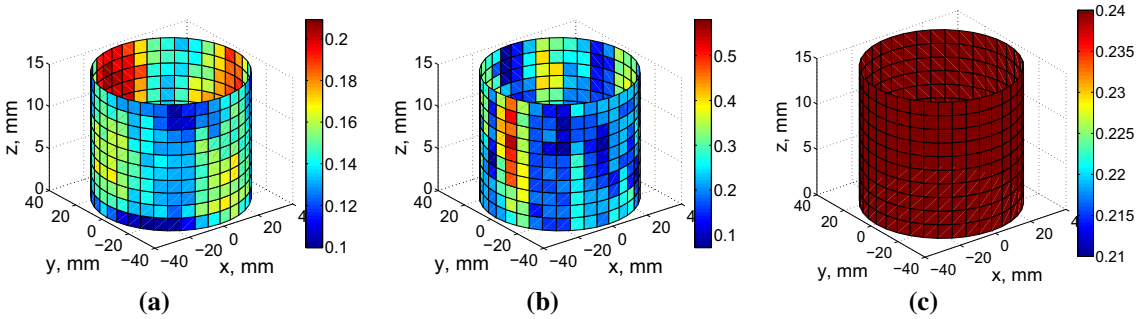

Fig. 18 Comparison of spatial variation of estimates of failure probability at the inner wall at $t = 35$ years for case 2. **a** Method 1. **b** Method 2. **c** Method 3

been discretized into—is significantly larger than in Method 1. This in turn demands higher computing costs and resources. It must be remarked here that as the FE discretization is made finer, the discretized system becomes a closer approximation to the physical system in terms of representation of both the displacement fields and the random fields, however, at a higher computational cost.

– *Method 3* Unlike Methods 1 and 2, here the spatial random inhomogeneities are neglected, and only the ensemble variations have been considered. This implies that the material properties have been modelled as random variables instead of as random fields, but having the same marginal pdf characteristics as the fields. Thus, here, no other meshing apart from FE discretization is required. Moreover, unlike in Method 2, the material properties have been taken to be the same for all the FE elements for a particular sample realization. It is obvious that the number of random variables entering the formulation is least in Method 3 and hence computationally cheapest.

Clearly, Method 2 is the most accurate of the three methods as the spatial random variabilities associated with the material properties are best modelled in Method 2 in the limit of mesh size approaching zero. However, the associated computational costs are highest in Method 2. Nevertheless, the accuracy of the results using Method 1 is examined vis-a-vis Method 2, which is treated as the benchmark. The predictions obtained by Method 3 are examined with respect to both Methods 1 and 2 to investigate the importance of random field modelling.

Figure 18 shows the spatial variation of the estimates of failure probability at the inner wall of the pipe for Case 2 at $t = 35$ years. An inspection of these Figures is quite revealing. Figure 18a shows that the locations concentrated around the OLE nodes have in general higher failure probabilities with respect to other locations. In contrast, the estimates obtained by Method 2 show no preferred concentration. In contrast, in Method 3 where the system is modelled as a random variable rather than a random field, the spatial variability of the damage is not captured at all. This example therefore highlights the importance of random field modelling in the analysis. Figure 19a shows a comparison of the pdf of damage at a location that corresponds to an OLE node for Case 2 at $t = 35$ years. We observe that the pdf of damage, using Methods 1 and 2, is in close agreement with each other. This highlights the accuracy of the proposed method. In contrast, the pdf of damage using Method 3 is significantly different, showing higher peaks but narrower tails. This observation is consistent with the earlier observation where the failure probability estimates obtained by Method 3 were observed to be smaller. Figure 19b shows a comparison of the pdf of damage at a location where no OLE nodes exist. Here, one can see that there are significant deviations between the predictions obtained from Methods 1 and 2. Here, one must remember that the discretized OLE field at non-OLE nodes is an approximation, and hence it is expected that there would be deviations from the predictions obtained from Method 2. Since in Method 3 the spatial variability is not modelled, the estimated pdf is identical to the Figure shown in Fig.19b and has not been included. Figure 20a shows a comparison of the estimated failure probability at a location that coincides with an OLE node, obtained for all three cases using all three methods. It is observed that the predictions from Method 1 and 2 are almost similar except in Case 3 where the proposed method overestimates the failure probability by a small percentage. This gives confidence on the accuracy of the results in the proposed method. In contrast, Method 3 significantly underestimates the failure probability for all three cases. This further illustrates that though Method 3 is computationally cheaper, it is not only incapable of capturing the spatial variabilities in damage, but also underestimates the failure probability. It is worth noting that the failure probability is higher in Case 2 than in the other two cases. In contrast, Fig. 20b shows the failure probability estimates at a location not coinciding with the OLE node. We see that the predictions by the proposed method are at variance with those

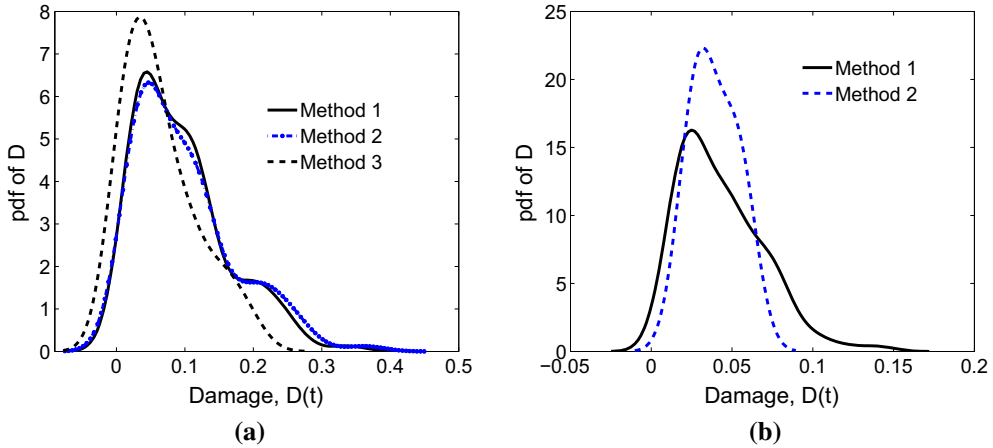

Fig. 19 Comparison of pdf of damage at $t = 35$ years for Case 2 **a** at an OLE node and **b** at a location in between OLE nodes

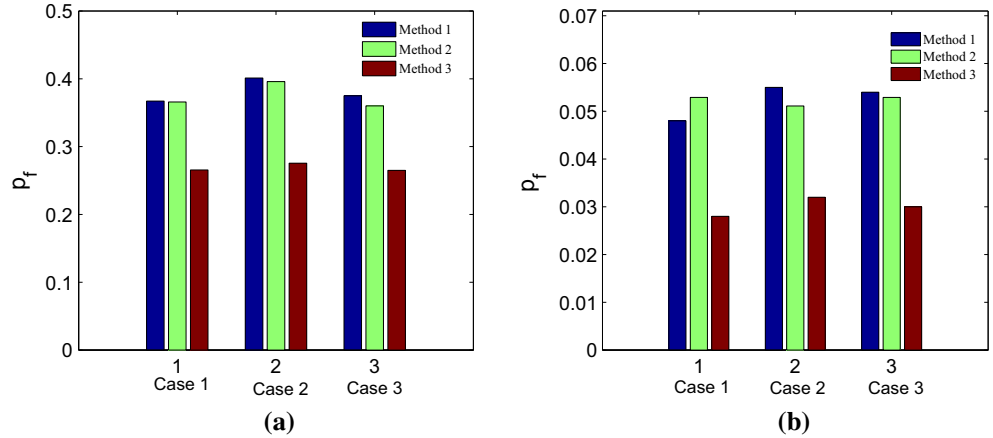

Fig. 20 Comparison of failure probability of damage at $t = 35$ years **a** at an OLE node and **b** at a location in between OLE nodes

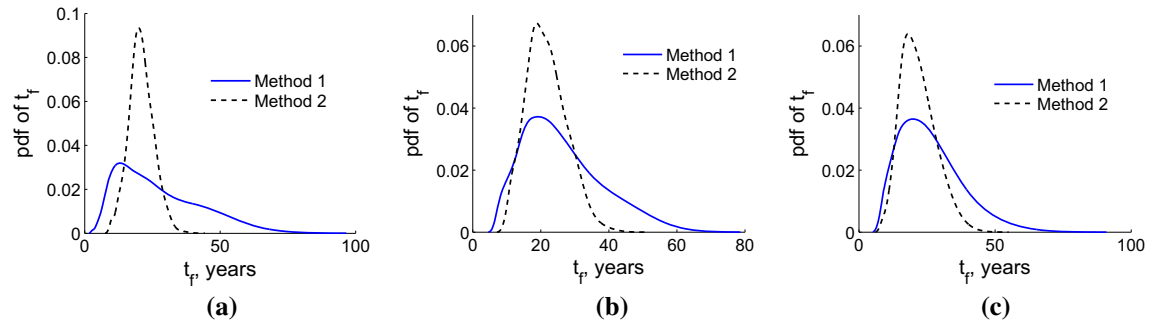

Fig. 21 Comparison of the pdf for time to failure obtained using Methods 1 and 2. **a** Case 1. **b** Case 2. **c** Case 3

obtained from Method 2. This is expected as the random field properties are not correctly represented where there are no OLE nodes. Nevertheless, one can see that the failure probability predictions are less conservative than in Method 3.

The time at which the creep damage attains the critical threshold value at any location within the spatial domain $\mathcal{R}$ is defined as the time to failure and denoted by t_f. Clearly, t_f is a random variable. Characterizing the pdf for t_f gives an indication of the lifespan of the structural component. Assuming $D_{cf} = 0.99$, the pdf of time to failure, t_f, is estimated for all the three cases and is shown in Fig. 21.

Here, the results of only Methods 1 and 2 are shown as the number of failures using method 3 with the sample size considered in this study was too small to estimate the pdf. An inspection of these Figures shows that the expected time to failure obtained from Methods 1 and 2 is almost identical in all the three cases. However, Method 1 shows a larger scatter in the predictions.

The computational cost associated with the three methods depends on the number of random variables entering the formulation. For case 2, where two material properties are modelled as random fields, the total number of random variables in Method 1 is 72, while in Method 2 the number of random variables is 8712. In contrast, the number of random variables in Method 3 is just 2. The savings in the computational costs in Method 1 are approximately 50% in comparison to Method 2. The additional computational cost associated with Method 2 can be attributed to the necessity for computing each of the elemental matrices having different numerical values for the material parameters. The computational cost associated with Method 3 is about 0.65 times the computational cost in Method 1, but has been shown to lead to significantly underestimating the failure probability.

8 Discussion

The proposed OLE-based methodology for a stochastic finite element analysis of a structure having spatial material uncertainties is an alternative approach to the more commonly used polynomial chaos (PC)-based formalisms presented in the literature. The PC-based formalism is a generalization of the Karhunen–Loeve (KL) series expansion. The KL series expansion is typically applicable (though not necessarily) for Gaussian processes where the basis functions are obtained by solving an integral eigenvalue problem, where the correlation function constitutes the kernel, and the projections are the Gaussian random variables. For non-Gaussian processes, the probability distribution of the projections has to be suitably defined. It has been shown mathematically that the KL series expansion is optimal implying that it requires the least number of terms in a series representation [17]. Obviously, a KL series representation of the random fields would lead to a minimum number of random variables entering the SFEM formulation and hence would be computationally most efficient. However, in the absence of a closed form representation of the correlation function, the basis functions can be evaluated only numerically by solving the integral eigenvalue problem. It was shown in [10] that the numerically evaluated basis functions do not necessarily lead to optimality. Instead, the authors showed that the expansion OLE (EOLE) method that uses KL expansion in conjunction with OLE to derive the basis functions leads to a more efficient discretization of random fields.

Extending the EOLE method for non-Gaussian fields is more difficult. Instead, it has been suggested [10] that a non-Gaussian process be first mapped to a Gaussian space and the transformed field be discretized into the Gaussian space using EOLE. Subsequently, the discretized non-Gaussian field is mapped back using memoryless translations [18]. The difficulty in this approach lies in estimating the autocovariance function of the field when transformed into the Gaussian space. This requires solving an integral equation [19]. Though analytical expressions for the upper bound for commonly used autocovariance functions have been derived in [19], a more generally applicable method is to use an iterative numerical algorithm [11]. However, as the discretization is carried out in the transformed Gaussian space, the optimality condition is not guaranteed upon transforming the fields back to the original non-Gaussian space. Moreover, the computational effort in estimating the autocovariance function in the transformed Gaussian space is non-trivial, and for some forms of autocovariance functions, it may not be possible to arrive at a convergent function.

A more general approach to KL representation of the random fields is to use PC expansions. Here, the basis functions are stochastic and are obtained as polynomials of basic random variables, and unlike in KL, the projections are deterministic. The form of the polynomial functions, and the distribution of the random variables are based on the Askey scheme and depend on the marginal pdf of the random field [17,20]. While this approach is straightforward for scalar random fields, extending the method to higher dimensions is fraught with difficulties. Moreover, constructing the PC representation of the random fields directly from measurement data involves significantly more computations [21]. On the other hand, the OLE approach discussed in this paper is simpler to implement.

9 Concluding remarks

A 3-D stochastic finite element formulation has been developed for the analysis of creep damage growth due to thermal effects in piping structures in industrial installations. The methodology incorporates into the FE

analysis the effects of spatial non-Gaussian inhomogeneities in the material properties. The optimal linear expansion scheme for a weak form representation of non-Gaussian fields has been generalized for 3-D cylindrical geometries and has been shown to preserve the non-Gaussian characteristics exactly at the nodes. A methodology has been presented on estimating the optimal shape functions that can be derived directly from the available data sets obtained from measurements. The methodology has been integrated with thermal creep damage growth equations to predict the most likely failure locations and their failure probability in a segment of a circular pipeline carrying high-temperature fluids. To the best of the authors' knowledge, this is the first study where principles of the stochastic finite element method have been used to characterize stochastic thermal creep damage.

Appendix: Creep damage growth equations

$$\frac{\mathrm{d}\varepsilon_{\mathrm{r}}^{\mathrm{c}}}{\mathrm{dt}} = A\frac{\sigma_v^{n-1}}{(1-D)^n}\left[\sigma_r - \frac{1}{2}(\sigma_\theta + \sigma_z)\right], \tag{31}$$

$$\frac{\mathrm{d}\varepsilon_{\theta}^{\mathrm{c}}}{\mathrm{dt}} = A\frac{\sigma_v^{n-1}}{(1-D)^n}\left[\sigma_\theta - \frac{1}{2}(\sigma_r + \sigma_z)\right], \tag{32}$$

$$\frac{\mathrm{d}\varepsilon_{\mathrm{z}}^{\mathrm{c}}}{\mathrm{dt}} = A\frac{\sigma_v^{n-1}}{(1-D)^n}\left[\sigma_z - \frac{1}{2}(\sigma_\theta + \sigma_r)\right], \tag{33}$$

$$\frac{\mathrm{d}\gamma_{\mathrm{r}\theta}^{\mathrm{c}}}{\mathrm{dt}} = \frac{3}{2}A\frac{\sigma_v^{n-1}}{(1-D)^n}\left[\tau_{r\theta}\right], \tag{34}$$

$$\frac{\mathrm{d}\gamma_{\theta\mathrm{z}}^{\mathrm{c}}}{\mathrm{dt}} = \frac{3}{2}A\frac{\sigma_v^{n-1}}{(1-D)^n}\left[\tau_{\theta z}\right], \tag{35}$$

$$\frac{\mathrm{d}\gamma_{\mathrm{rz}}^{\mathrm{c}}}{\mathrm{dt}} = \frac{3}{2}A\frac{\sigma_v^{n-1}}{(1-D)^n}\left[\tau_{rz}\right]. \tag{36}$$

In the above equations A, n are the creep constants for the given pipe material. In all of the above equations, the expression for the effective stress, also termed as the von Mises stress, $\sigma_v(t)$ is given by

$$\sigma_v(t) = \frac{1}{\sqrt{2}}\sqrt{\left[(\sigma_r - \sigma_\theta)^2 + (\sigma_\theta - \sigma_z)^2 + (\sigma_z - \sigma_\theta)^2\right]}. \tag{37}$$

References

1. Woo, C.W., Li, D.L.: Statistical analysis of material damage with changing internal structure. Eng. Frac. Mech. **45**, 245–254 (1993)
2. Der Kiuregian, A., Ke, J.B.: The stochastic finite element method in structural reliability. Prob. Eng. Mech. **3**, 83–91 (1988)
3. Ghanem, R.G., Spanos, P.D.: Stochastic Finite Elements: A Spectral Approach. Springer, London (1991)
4. Kleiber, M., Hien, T.D.: The Stochastic Finite Element Method: Basic Perturbation Technique and Computer Implementation. Wiley, New York (1992)
5. Manohar, C.S., Ibrahim, R.A.: Progress in structural dynamics with stochastic parameter variations. App. Mech. Rev. **52**, 177–197 (1999)
6. Haldar, A., Mahadevan, S.: Reliability Assessment Using Stochastic Finite Element Analysis. Wiley, New York (2000)
7. Sudret, B., Der Kiureghian, A.: Comparison of finite element reliability methods. Prob. Eng. Mech. **17**, 337–348 (2002)
8. Xiu, D.: Numerical Methods for Stochastic Computations: A Spectral Method Approach. Princeton University Press, Princeton (2010)
9. Kaminski, M.: The Stochastic Perturbation Method for Computational Mechanics. Wiley, Chichester (2013)
10. Li, C.-C., Der Kiureghian, A.: Optimal discretization of random fields. J. Eng. Mech. ASCE **119**, 1136–1154 (1993)
11. Gupta, S., Manohar, C.S.: Dynamic stiffness method for circular stochastic Timoshenko beams: response variability and reliability analysis. J. Sound Vib. **253**, 1051–1085 (2002)
12. Sasikumar, P., Suresh, R., Gupta, S.: Stochastic finite elements of layered composite beams with spatially varying non-Gaussian inhomogeneities. Acta Mech. **225**, 1503–1522 (2014)
13. Boyle, J.T., Spence, J.: Stress Analysis for Creep. Butterworths Co., London (1983)
14. Kachanov, L.M.: Introduction to Continuum Damage Mechanics. Martinus Nijhoff, Leiden (1986)
15. Penny, R.K., Marriot, D.L.: Design of Creep. McGraw-Hill Book Co., London (1980)
16. Zhou, C., Tu, S.: A stochastic computation model for the creep damage of furnace tube. Int. J. Press. Vessels Pip. **78**, 617–625 (2001)

17. Xiu, D., Karniadakis, G.E.: The Wiener–Askey polynomial chaos for stochastic differential equations. SIAM J. Sci. Comput. **24**, 619–644 (2002)
18. Grigoriu, M.: Crossings of non-Gaussian translation processes. J. Eng. Mech. ASCE **110**, 610–620 (1984)
19. Der Kiureghian, A., Liu, P.L.: Structural reliability under incomplete probability information. J. Eng. Mech. ASCE **112**, 85–104 (1986)
20. Wiiteven, J.A.S., Sarkar, S., Bijl, H.: Modeling physical uncertainties in dynamic stall induced fluid-structure interaction of turbine blades using arbitrary polynomial chaos. Comput. Struct. **85**, 866–878 (2007)
21. Das, S., Ghanem, R., Finette, S.: Polynomial chaos representation of spatio-temporal random fields from experimental measurements. J. Comput. Phys. **228**, 8726–8751 (2009)